Experience-based noise model of infrared detectors for system dimensioning and simulation

Alain Kattnig, Christian Musso

Infrared Physics & Technology 142 (2024) 105589

Contents lists available at ScienceDirect

Infrared Physics and Technology

journal homepage: www.elsevier.com/locate/infrared

Research Paper

Experience-based noise model of infrared detectors for system dimensioning and simulation

Alain Kattnig *, Christian Musso

DOTA, ONERA, Université Paris-Saclay, Palaiseau 91120, France

ARTICLE INFO

Keywords:
Noise
Model
Infrared detector

ABSTRACT

We show that infrared detectors frequently exhibit non-Gaussian spatial noise, which makes it difficult to compare their performance. The power-law-like behavior we show can be very detrimental to certain detection missions, hence the need to characterize this noise. We demonstrate that a simple mixture of Gaussian and Student processes corresponds to the observed example, and that the parameter determination procedure described here reaches its theoretical limit.

1. Introduction

Before they can be used in an imaging system, infrared detectors must be characterized as a sub-system. There are many parameters of interest, but here we are interested in the noise affecting these detectors. Because this quantity is just as important as the radiometric sensitivity of a system. It is indeed the denominator of the signal to noise ratio, but if the signal can be clearly defined, such is not the case of the noise quantity.

Indeed, we assume too quickly that many noises can be reduced to temporally and spatially independent Gaussian processes [1].

Unfortunately, uncontrolled variations in manufacturing or environmental parameters, as well as poorly understood phenomena such as Random Telegraph Pixels [2] leads to non-gaussian noise in infrared detectors responses. This does not prevent us from using indicators that are supposed to characterize noise, such as standard deviation. But, whether we like it or not, standard deviation is associated in our minds with the Gaussian distribution. This leads to two pitfalls, the first relating to the estimation of the standard deviation and the second to its misuse.

Indeed, the reference estimator of the standard deviation is not robust to outliers [3]. However, these outliers are numerous to very numerous depending on the infrared detector technology. As a consequence, robust estimators are used in a more or less hidden way.

We say hidden, because removing misbehaving detectors from the sample is simply a way to make the estimator more robust.

Once the value of the standard deviation is obtained, it is likely to be used as if the underlying statistic was Gaussian in all calculations of range, detection probability and other imaging performance indices. This is not an unreasonable assumption, but at the very least it must be done in full knowledge.

Thus, we propose here to build a noise probability model that simply accounts for the intrinsic existence of outliers in outputs of infrared detectors. The returned parameters will allow to fully characterize the majority behavior of detectors as well as characterizing the behavior of outliers.

These parameters will be measured using an optimization algorithm, which makes the evaluation of its quality all the more necessary. To this end, we will compare the performance of the proposed estimator with the theoretical lower bound.

2. Noise definition

In practice, we're dealing with two types of noise in imaging: temporal noise, which corresponds to temporal variations in the response of a single detector, and spatial noise, which corresponds to variations in the response from one detector to another.

In most cases, the spatial noise [4] is much more important than temporal noise and cameras must undergo spatial calibration to reduce it as much as possible.

2.1. Spatial calibration

Because of the inhomogeneities of response of infrared detectors, it is often necessary to correct them. This is typically done by presenting scenes of different homogenous luminance, typically from blackbody,

* Corresponding author.
E-mail address: alain.kattnig@onera.fr (A. Kattnig).

https://doi.org/10.1016/j.infrared.2024.105589
Received 26 June 2024; Received in revised form 24 September 2024; Accepted 5 October 2024
Available online 9 October 2024

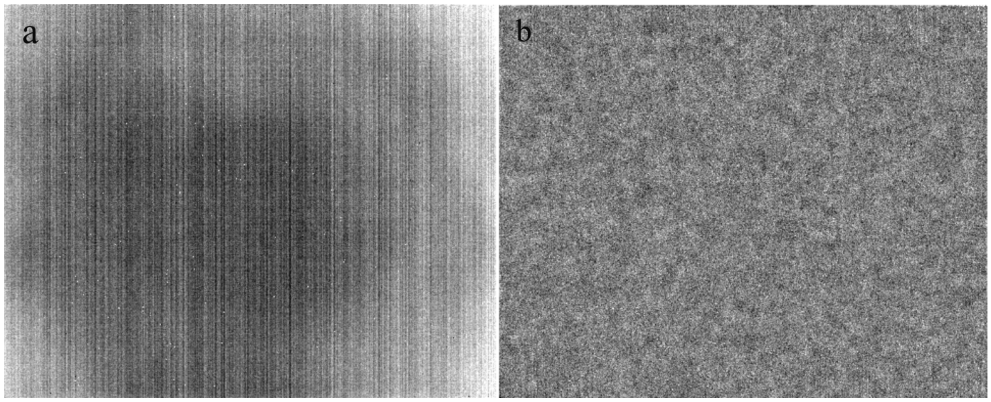

Fig. 1. on a) we find the image of the black body at 10 °C after affine correction of inhomogeneities on a dynamic range equal to [-0.6, 1] mV. On b) we find the same image after removal of columns as well as large scale variations. Its dynamic range is equal to [-0.3, 0.3] mV. To be able to see an image, outlier pixels have been bounded for this representation.

and by imposing an identical radiometric behavior on all detectors [5,6]. This constraint results in an affine correction to be performed on each detector of the array. Most of the time, these operations are done on the temporal averages of the measurements, in order to take into account only the spatial contribution to the noise.

The linear regression used to determine the correction coefficients is an operation that amplifies the spatial noise affecting the original measurements (not the temporal noise). And when the spatial stability assumptions of the parasitic flux and electrical offset voltage are violated [4], spatial artifacts will appear in the images thus corrected. These artifacts will necessarily be residuals of erroneous gain and/or offset correction. In order to avoid characterizing these artifacts, which are not intrinsic properties of the physics of photoelectric detection, we have sought to remove them as best we can.

For this we estimate and remove columns, characteristic of the voltage defects of the readout circuits, as well as polynomials of degree 3 of 1/20th image size overlapping windows to model the main residual variations of the gain (in Fig. 1).

The examples used in this article come from a commercial high-end MWIR component of 640 × 512 pixels with a 15 μm pixel size that we arranged in a cryostat. This component took images of a black body with 18 different temperatures between 10 and 43 °C, which are used to correct for spatial inhomogeneities [5].

We thus retained only the statistical variations which are intrinsic to the detector and not related to the variations of supply voltage of the circuit of reading of the detector or the variations of the conditions of infra-red lighting inside or around the cryostat [7,8]. We assume that the whole process results in a spatially stationary and ergodic random variable. The assumption of stationarity is reasonable, as this is the ultimate goal of all infrared detector manufacturers and because residual non-uniformities are then corrected by signal processing.

As for the ergodicity hypothesis, it is indispensable for any practical study. However, as the detector matrix is a unique phenomenon of limited extension, the ergodicity hypothesis is difficult to test.

As far as units are concerned, we've chosen not to use them explicitly, as there are a wide variety of units used to record their detector's measurements, from the digital count to the volt, millivolt or pico-ampere, one of our favorites. What's important here is the statistical distribution of measured values, not their units or absolute values. For this reason, all the following figures show image values without units.

3. Probability density function model and estimation

It is first necessary to experimentally observe the probability law of corrected blackbody images. This is not so straightforward, because of the very large amplitude of the image values. This amplitude imposes the use of a logarithmic representation, which in turn imposes the use of positive values only. In the following, we will therefore analyze separately the positive and negative parts of the data set.

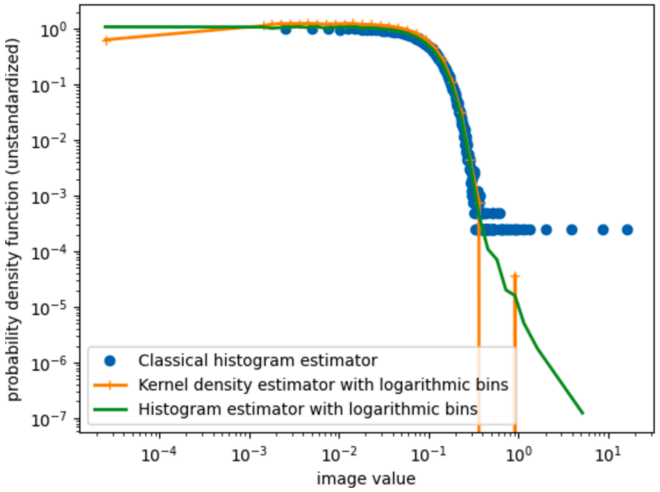

Fig. 2. Comparison of three different estimators of the probability density function over a data probability range of 7 orders of magnitude.

3.1. Visualization of the probability density function

Indeed, since the probability of occurrence of intense events is rare, the probability density estimator must be chosen carefully. Both the classical histogram method and the kernel density estimator fail to measure the probability density of the rarest events, because they use fixed-size bins.

We therefore modified these methods by choosing logarithmically distributed counting intervals as in Alstott's paper [9]. The size of these intervals increases with their value, thus compensating for the sparsity of the events when their value increases.

Finally, to prevent empty intervals from interfering with log–log representations and the perception of power-law distributions, we had to deal with empty bins in the histogram.

Since we shouldn't adapt the intervals to the data, we chose to double the following intervals when they are empty. This process is repeated each time an empty bin is encountered. In this way, we avoid empty bins without unduly adapting a given realization of the observed random variable. A comparison of these methods is given in Fig. 2.

It is important to note that the power law decay observed in this figure is only really observable with the histogram estimator with logarithmic bins. However, in this representation, the classical laws are not

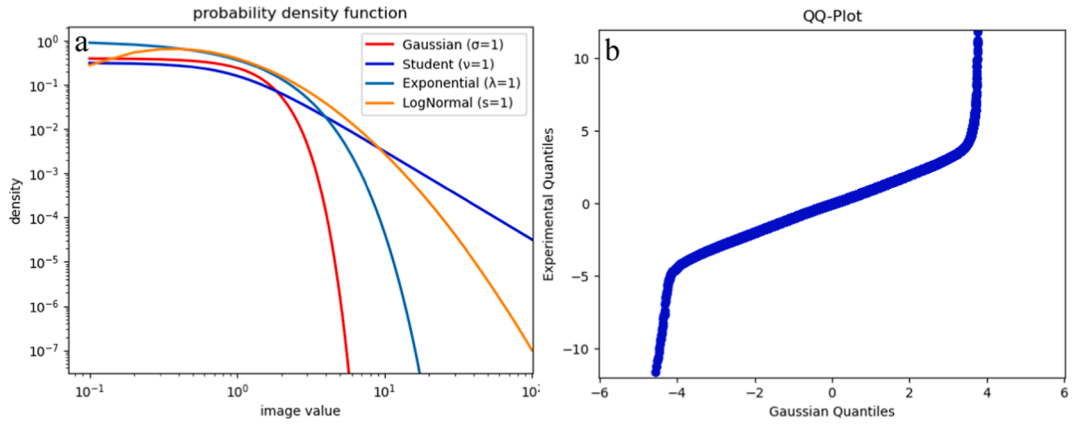

Fig. 3. a) comparison of four classical probability density functions in a log–log plot. b) a QQ-plot to compare an experimental statistic with a theoretical Gaussian statistic.

recognizable, so we give in Fig. 3a their representation in a log–log graph.

We have every theoretical reason to believe that the Gaussian probability density law is the best fit to represent most of the data. Let us demonstrate this by comparing the quantiles of the Gaussian statistic with those of the experimental statistic (in Fig. 3b).

This shows that up to four standard deviations, the distribution of the experimental data corresponds perfectly to a Gaussian. It is now a question of determining which law to use to model the behavior of the dataset at the highest values.

The next step is to determine the law to use to model the behavior of the data set at higher values. First, it is important that the behavior of this law does not disturb the behavior at low values. Thus, the LogNormal law cannot be chosen despite its correct power law behavior. This led us to choose the student law among the classical laws, because of its parametric power law asymptotic behavior and its compatibility with the Gaussian law (in Eq. (1)).

$$t(x,\nu) = \frac{\Gamma\left(\frac{\nu+1}{2}\right)}{\sqrt{\pi\nu}\,\Gamma\left(\frac{\nu}{2}\right)}\left(1+\frac{x^2}{\nu}\right)^{-\frac{\nu+1}{2}} \tag{1}$$

t being the student probability density law where ν is the number of degree of freedom (abbreviated as df). This definition leads to a $x^{-\nu}$ asymptotic behavior.

3.2. Modeling the experimental distribution by a mixture distribution

The mixture distribution is a powerful tool, allowing to combine any probability distribution. As we recognized both a Gaussian and a Student behaviour in the experimental probability distribution function (pdf), we choose to use a mixture of these two pdf.

$$\pi_\theta(x) = \alpha\varphi_{0,\sigma^2}(x) + (1-\alpha)\frac{1}{\sigma}t\left(\frac{x}{\sigma},\nu\right)$$

where

$$\varphi_{\mu,\sigma^2}(x) = \frac{1}{\sqrt{2\pi}\sigma}e^{-\frac{(x-\mu)^2}{2\sigma^2}} \tag{2}$$

is the Gaussian pdf of mean μ and standard deviation σ.

Sample from this mixture is easy. In practice, such a random variable is obtained by a random choice of drawing from one (with probability α) or from the other distribution (with probability (1-α)).

Here, we chose the scale parameter of the Student distribution to be equal to the standard deviation parameter of the Gaussian distribution in order to mimic as much as possible the behavior of the Gaussian distribution for values less than the standard deviation. First fits gave encouraging results (in Fig. 4) which validate the model, since most of experimental probability density do show such behavior.

At this point, we need to build the best possible estimator for the

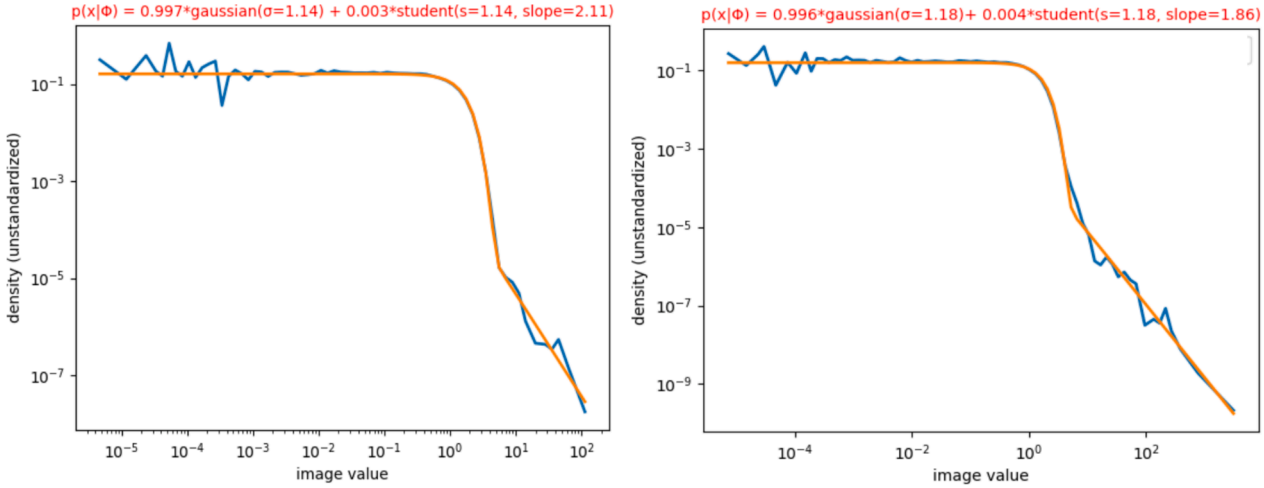

Fig. 4. The result of a curve fit parameter optimization on two blackbody measures at 10 °C with a commercial MWIR camera. In blue, we give the histogram estimation against the model computed on data (in orange). Parameters of the model are given in red above the plot. The slope is ν and s is equal to σ.

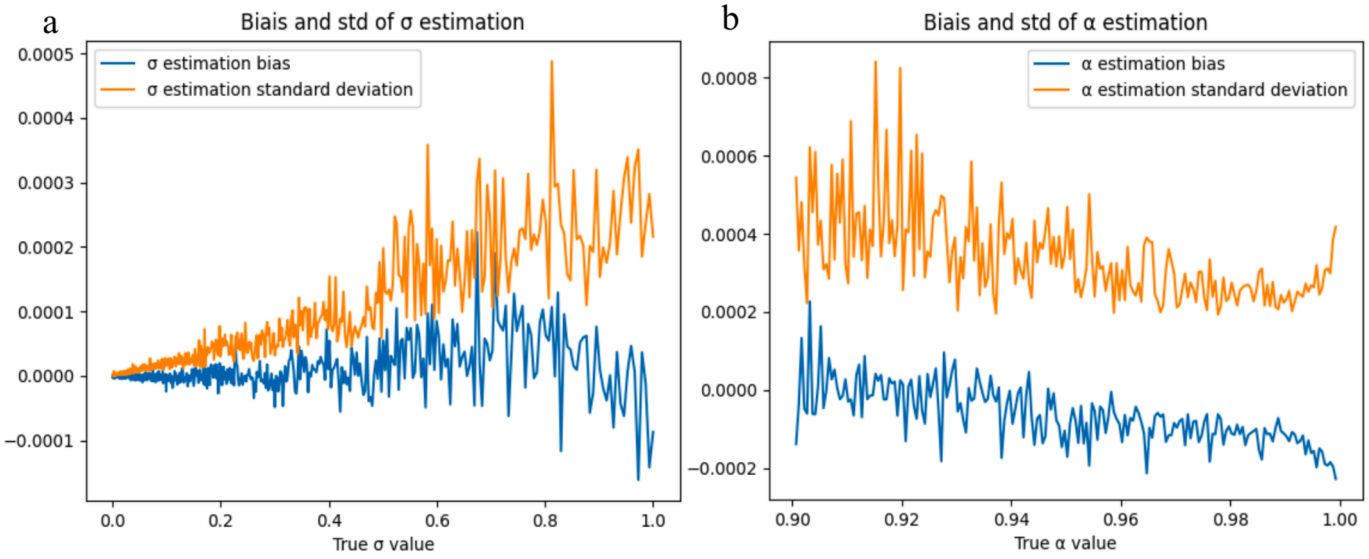

Fig. 5. Bias and standard deviation of the estimator of α (in b) and σ (in a) parameter of the model versus their value.

three parameters of the model. The simplest solution being the Maximum likelihood, we'll study its properties and optimality.

3.3. Maximum likelihood estimator

This method consists of maximizing the likelihood with respect to all three parameters of pdf mixture. Using a sample from the mixture, the likelihood is expressed as follows:

$$L_\theta(\mathrm{X}) = \prod_{i=1}^{n} \pi_\theta(x_i) \text{ with } \theta = (\alpha, \sigma, \nu) \text{ and } X = (x_1, x_2, \ldots, x_n)$$

In practice, this involves taking the logarithm of the product of the probability densities calculated for each sample in the draw and for the parameters explored. This leads to the maximum likelihood estimator of Eq. (3):

$$\widehat{\theta}_n = \underset{\theta \in \Re^3}{\operatorname{argmax}} \sum_{i=1}^{n} \log(\pi_\theta(x_i)) \tag{3}$$

This optimization can be solved using standard optimization routines like the L-BFGS-B [10] algorithm. The performance of the Maximum Likelihood method will be evaluated by comparing the standard deviation of the parameter estimates with a theoretical lower bound.

3.3.1. Computation of the Cramér-Rao lower bound

Fortunately, it is possible to compute this theoretical bound directly through the derivation of the Cramér-Rao bound. It needs the computation of the inverse of the Fisher Information Matrix (in Eq. (4)).

$$J_\theta = \mathrm{E}\left[\left(\frac{\partial}{\partial\theta}\log(\pi_\theta(X))\right)\left(\frac{\partial}{\partial\theta}\log(\pi_\theta(X))\right)^T\right] \tag{4}$$

E denotes the expectation with respect to the random variable X, which follows the probability density function (pdf) π_θ. The Cramer-Rao bound with n i.i.d samples x_i from π_θ is as follows (in Eq. (5)).

$$CRB_\theta = \frac{1}{n} J_\theta^{-1} \tag{5}$$

It gives the minimal covariance matrix of any estimator of θ with n measurements. The information matrix J_θ is approximated by Monte Carlo simulations using N samples x_i from π_θ.

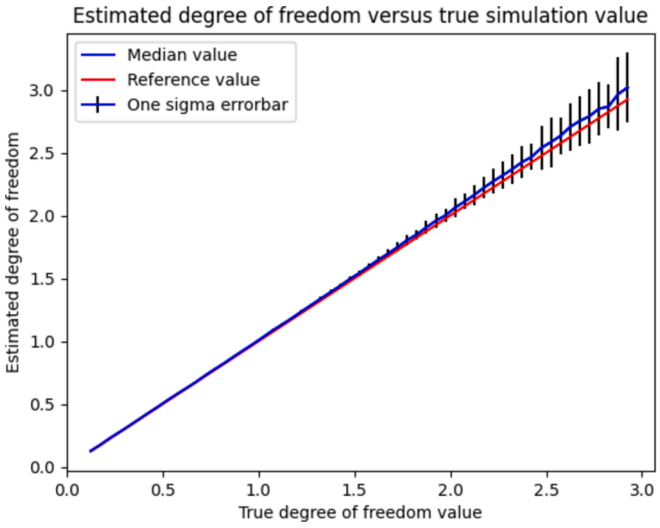

Fig. 6. Plot of the median of the estimated degree of freedom against its true value with the error bar equal to the standard deviation of the estimator.

$$J_\theta \approx \frac{1}{N}\sum_{i=1}^{N} \mathrm{E}\left[\left(\frac{\partial}{\partial\theta}\log(\pi_\theta(x_i))\right)\left(\frac{\partial}{\partial\theta}\log(\pi_\theta(x_i))\right)^T\right] \tag{6}$$

It is then sufficient to calculate the derivatives of π_θ versus α, σ and ν to build the Fisher Matrix. We give in the Appendix the details of theses calculus.

Let's check how close we are to the practical performance of the maximum likelihood estimator.

3.3.2. Performances of the experimental maximum likelihood estimator on a realistic test case

In order to study the behavior of the estimator of these parameters, we simulated numerous measurements of a mixed distribution of Gaussian and Student distributions. As we have prior knowledge of the likely value of these parameters in the wild, we have restricted the parameter space as follows:

– ν is uniformly taken between 0.1 and 3, corresponding to a slope of 1.1 to 4.

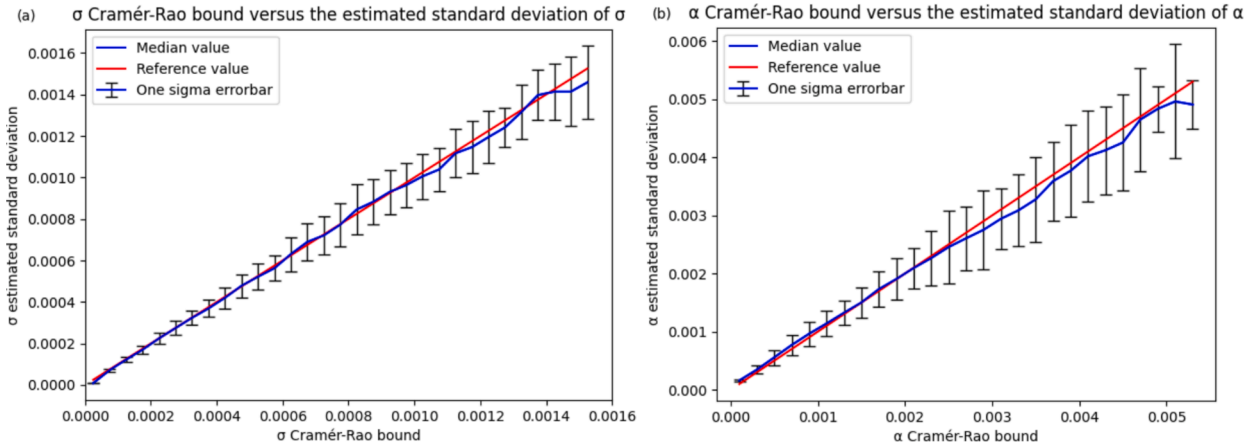

Fig. 7. On the left, comparison of the Cramér-Rao bound on σ with the estimated standard deviation of σ, the standard deviation is proportional to σ (roughly 11% of its value). On the right, comparison of the Cramér-Rao bound on α with the estimated standard deviation of α, the standard deviation is proportional to α (roughly 19% of its value).

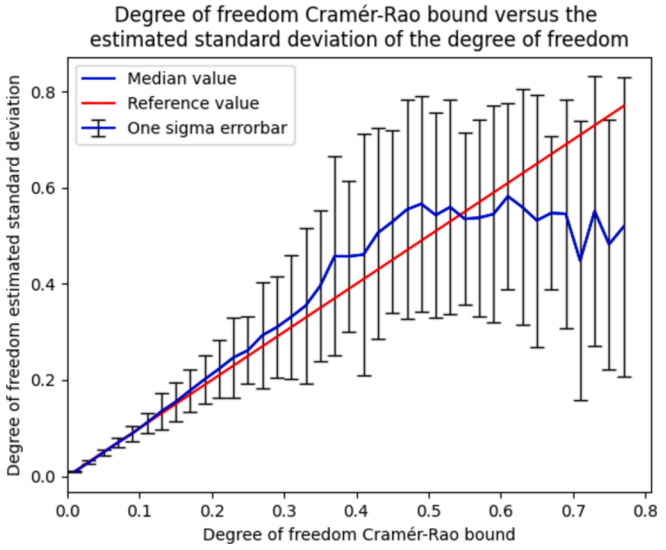

Fig. 8. Comparison of the Cramér-Rao bound on the degree of freedom with its estimated value. The standard deviation is not proportional to the degree of freedom value.

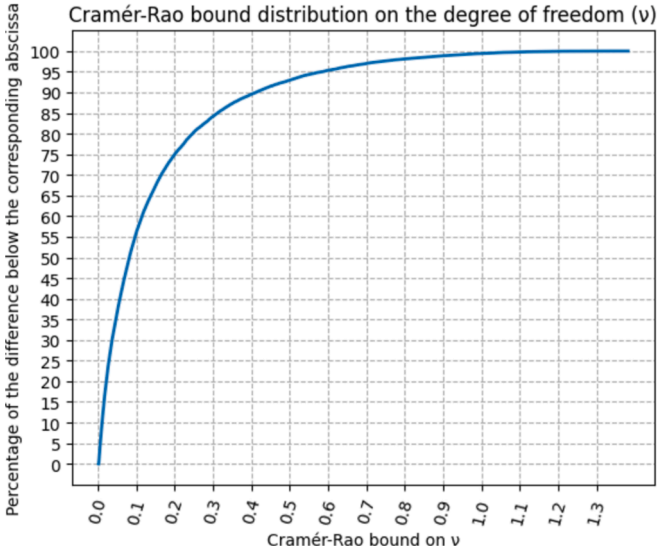

Fig. 9. Experimental distribution of the values of the Cramér-Rao bound.

– 1-α is logarithmically uniform between 10^{-1} and 10^{-3}, not too far from 1 since the Gaussian distribution should be dominant.

– σ is logarithmically uniform between 10^{0} and 10^{-3}.

For the choice of the number of samples we took a classical Infrared detector size of 512*640 and drew 50 realizations each time before computing the mean and the standard deviation of the estimators of α, σ and ν. We also computed the Cramér-Rao bound for each realization.

We first give in Fig. 5 the bias and standard deviation of σ and α estimation while showing in Fig. 6 the estimation versus the true ν value.

The fit of these two parameters is very satisfactory, but the degree of freedom fit is more problematic (in Fig. 6).

Indeed, the variance of the estimation of the later parameter is much higher than that of the two preceding parameters. However, there are objective reasons for this: firstly, as we have a mixture with a large Gaussian majority, any robust variance estimator will provide the correct Gaussian variance.

Secondly, as the Gaussian density function decreases exponentially, gaussian outliers can be easily identified and numbered to calculate the mixing ratio of Gaussian and Student.

But estimating the degree of freedom of the Student part of the mixing is obviously much more difficult. It involves rare values, the number of which decreases as the degree of freedom increases, which explains the poor quality of this estimator for high values of the degree of freedom.

3.3.3. *Optimality of the estimator*

Having calculated the Cramér-Rao bounds for our estimators, we are now interested in the performance of the optimizer used in practice in relation to this performance limit. We chose the L-BFGS-B method for its performance and speed compared with the other methods available.

The question is therefore whether its performance reaches the theoretical limit. Remember that for reasons of computing power, we had to limit ourselves to drawing 50 different realisations for each triplet of parameters. As a result, the standard deviation of the measurement will have a limited performance.

Having said that, let's look at the performance of our estimator in relation to the Cramér-Rao bounds (in Figs. 7 and 8).

We are pleased to note that the performance of our estimator is in line with the theoretical limit, even if the statistical variations can be quite high. It remains to analyse the quality of the estimator of the degree of freedom of the Student mixture distribution. We have already seen in the comparison with the simulated value in Fig. 6 that the degree

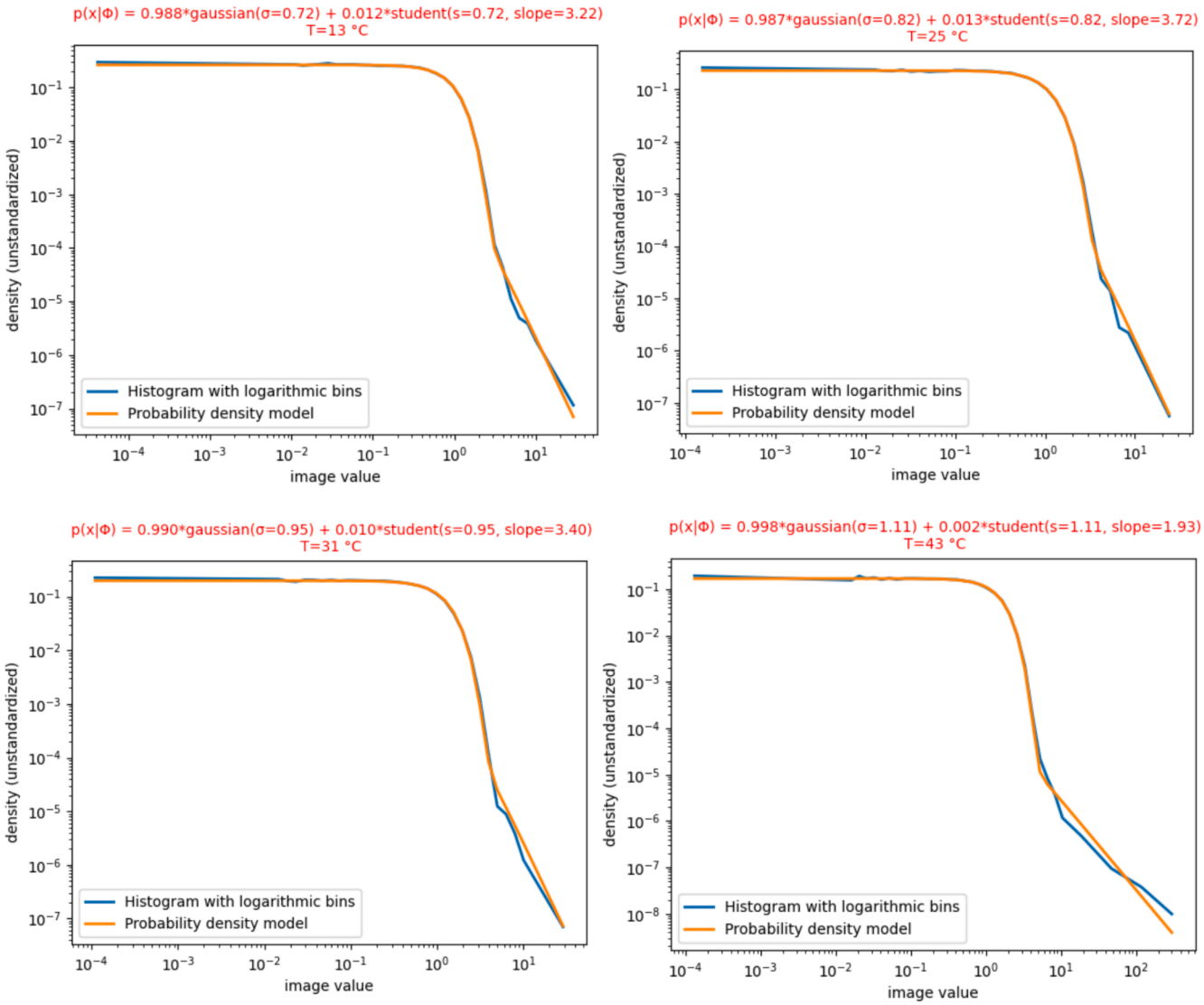

Fig. 10. Comparison of our probability density model fitted on measures of a blackbody at four different temperatures with our experimental estimator of the probability density (i.e Histogram with logarithmic bins).

of freedom parameter was less well estimated than the others were. We can therefore expect poorer results (in Fig. 8).

This time, the correspondence between the two values no longer seems certain and the standard deviation of the estimator is very high compared with the value of the parameter. But let's see if the problematic values of the Cramér-Rao bound on the degree of freedom are significant. To do so we show in Fig. 9 the distribution of the values of this bound on our database.

This figure shows that, in 75 % of cases, the bound is less than 0.2, a range in which the agreement between the Cramér-Rao bound and the estimate of Fig. 8 is quite satisfactory.

We can therefore conclude that the optimisation scheme we have chosen has reached its theoretical limit and is therefore optimal.

4. Benefits and use of this new noise model

Any improvement in physical understanding is beneficial in itself, but we can already show how it might improve the current situation when designing or using infrared detectors. Here, we develop two different types of use.

4.1. Comparing performances

With this model, we hope to help solving the problem of comparing the performance of infrared detector arrays. The sensitivity of a matrix of infrared detectors is often limited by the residual fixed spatial noise, and this noise is most of the time only characterized by the calculation of a standard deviation. Even if this parameter has nothing to do with the uniform distribution, in practice we usually make the over-simplifying assumption that we are indeed in the presence of this type of distribution.

However, as the presence of outliers deeply disturbs the calculation of the standard deviation, different laboratories and manufacturers have implemented different protocols for measuring the residual fixed spatial noise[11].

These protocols typically exclude pixels according to certain criteria or use robust statistics that only measure the majority (Gaussian) part of the detectors' statistical behavior.

It is therefore impossible to make a valid comparison without having access to the original data, which is often unreachable.

On the other hand, the outputs of our model will allow us to characterize the Gaussian behavior of the majority of the matrix by providing its standard deviation. In addition, we will obtain the number of pixels

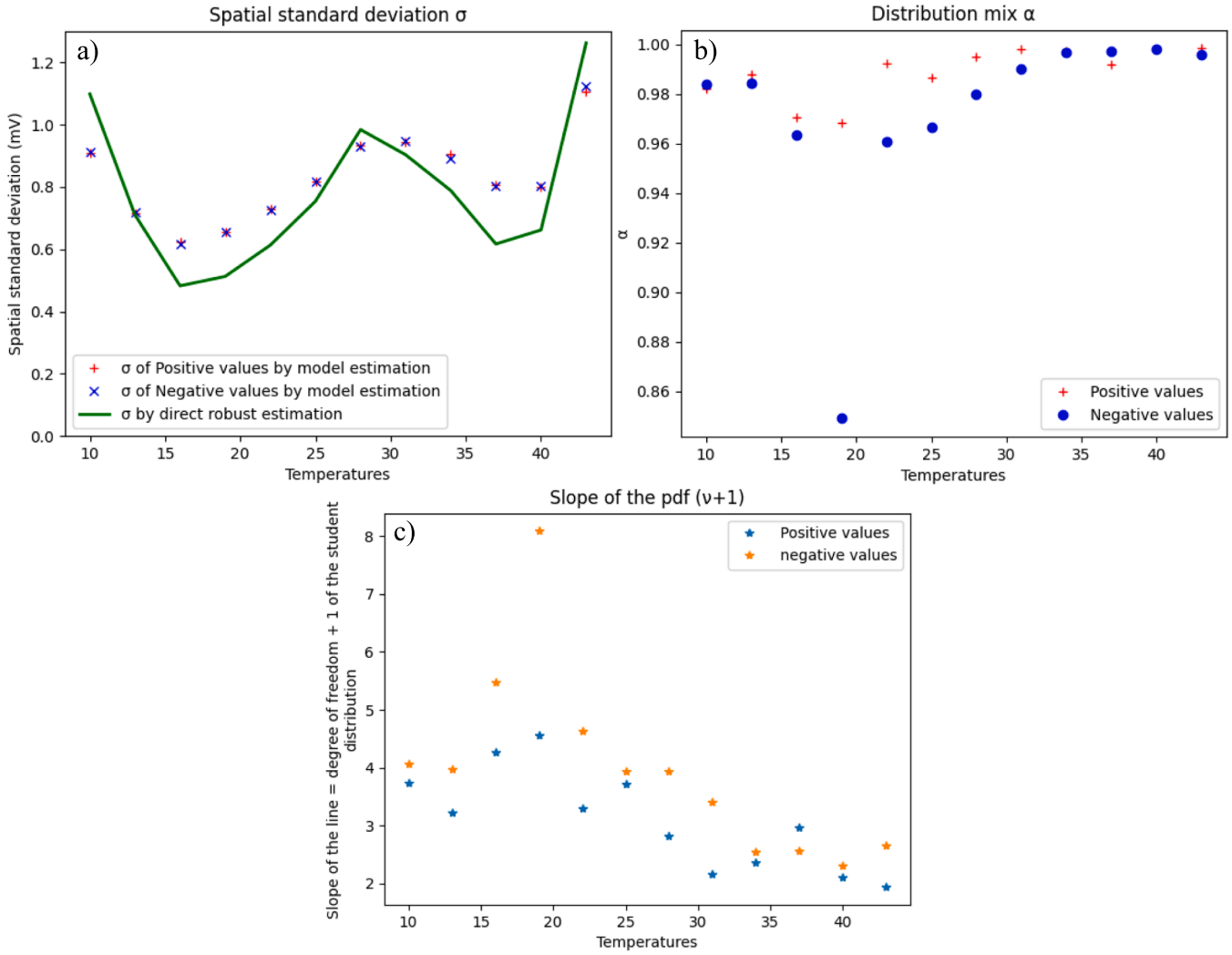

Fig. 11. Comparison of probability density parameters for blackbody measures at different temperatures. We separated the data between negative and positive values by subtracting the data median. In figure a) we added another measure of the standard deviation by robust estimation for reference.

obeying a different law through the mixing parameter (including RTS). As for the number of degrees of freedom, this characterizes the severity of the perturbation induced, and eventually could be used to infer some RTS properties.

4.2. System dimensioning and simulation

Infrared sensors are often used to detect unresolved objects, for example in missile warning systems or tracking systems. These missions are very sensitive to the rate of outliers, which are modeled by the parameters of the student part of our model.

The introduction of models that are more faithful to reality will therefore enable detection processes to be better dimensioned.

Realistic image simulations will also be very useful for pre-testing the reliability of the processing pipeline, whether for simple image production or other image parameter extraction.

4.3. Consequences

Unfortunately, the era of "universal" performance comparisons is becoming increasingly remote, as the recognition of the "normality" of outliers means that the observation mission [12] assigned to the detector will strongly determine its sensibility to outliers.

Thus, a strategic or tactical view of the battlefield will tolerate many outliers while a missile warning system will generate too many false alarms, paralyzing the whole system.

5. Example

We have applied our model to a sequence of blackbody measurements ranging from 10 °C to 43 °C using a MWIR detector at 80 K (detector temperature). The measurements are then spatially corrected by an affine function estimated over the whole temperature range.

As we are interested in outliers, we had to take extreme care to eliminate dead or saturated pixels from the estimators. Once done, we give in Fig. 10 several examples of the result of the probability density model alongside the logarithmic bins histogram estimator for different sample images taken at several blackbody temperatures.

There is a good agreement between the model directly estimated from the data and the histogram estimator we built. Now, in order to validate our results we separated each set of data into positive and negative values after removing the median and applied separately our probability density model. Except for extremely low photon-counting instrument [13], we should measure similar behavior for negative and positive value. This is a simple yet efficient way to test the quality of the estimator.

We show in Fig. 11 the distribution of all model parameters as a function of the measured blackbody temperature.

Experimental results confirm the theoretical findings that the standard deviation is best estimated, while the distribution mix and the degree of freedom parameters lacks behind.

The important spread of the degree-of-freedom estimations demonstrates the interest of computing the Cramér-Rao bound. In our example, its low reliability means that more data are needed to use the value of the degree-of-freedom for anything other than an order-of-magnitude assessment.

In practice, it's not very difficult to acquire more data to compensate for the weakness of the estimator, once it's known. However, to do this, we need to guarantee that we will get truly independent measurements, especially for the "anomalous" part of the noise model: Student's law.

There are two ways of achieving this: one is to modify the incident flux, thus covering another part of the dynamic range in which several detectors may behave differently. The other is simply to wait a certain amount of time before each new acquisition. Indeed "anomalous" detectors have time-dependent properties, the best-known example being "Random Telegraph Signal" (RTS) detectors [1,3] whose response to flux fluctuates in time between two or several states.

But it is up to the analyst to demonstrate the independence of these additional measures.

6. Conclusions

In our search for a model of the noise behavior of infrared detectors, we had to refine an histogram estimator, making it capable of revealing power-law behavior. Since we have repeatedly observed this power-law behavior in our experiments with noise in infrared detectors, we proposed as a model a simple mixture of Gaussian and Student probability distributions.

We then developed an estimator of the three parameters of this model and demonstrated that its performance reaches the theoretical limit given by the Cramér-Rao bounds.

Several examples have been given in which the model fits our histogram estimator and performs correctly against an unrelated standard deviation estimator and after a data split.

Credit authorship contribution statement

Alain Kattnig: Writing – original draft. **Christian Musso:** Writing – review & editing.

Declaration of competing interest

The authors declare that they have no known competing financial interests or personal relationships that could have appeared to influence the work reported in this paper.

Data availability

Data will be made available on request.

Acknowledgements

We would like to thank all the members of the laboratory who have carried out the numerous characterisations of infrared detectors on which we have relied here.

We would also like to thank the anonymous reviewers for their time and effort in reviewing the manuscript. We sincerely appreciate all the valuable comments and suggestions that helped us to improve the quality of the manuscript.

Appendix A

The derivatives of π_θ are given below in Eqs. (8) and (9).

$$\begin{aligned}
\frac{d\pi_\theta}{d\alpha} &= \varphi_{0,\sigma^2}(x) - \frac{1}{\sigma} t\left(\frac{x}{\sigma},\nu\right)\\
\frac{d\pi_\theta}{d\sigma} &= \alpha\frac{d\varphi}{d\sigma} - \frac{(1-\alpha)}{\sigma^2}\left[t\left(\frac{x}{\sigma},\nu\right) + \frac{x}{\sigma}\frac{d}{d\sigma}\left[t\left(\frac{x}{\sigma},\nu\right)\right]\right]\\
\frac{d\pi_\theta}{d\nu} &= \frac{(1-\alpha)}{\sigma}\frac{d}{d\nu}\left[t\left(\frac{x}{\sigma},\nu\right)\right]
\end{aligned} \tag{8}$$

With.

$$\begin{aligned}
\frac{d\varphi}{d\sigma} &= \frac{(x-\nu-\sigma)(x-\nu+\sigma)}{\sqrt{2\pi}\sigma^4} e^{-\frac{(x-\mu)^2}{2\sigma^2}}\\
\frac{d}{d\sigma}\left[t\left(\frac{x}{\sigma},\nu\right)\right] &= -\frac{x}{\sigma^2}\left[\frac{dt}{dx}\right]\left(\frac{x}{\sigma},\nu\right)\\
\text{and } \frac{dt}{dx} &= -\frac{2x\Gamma\left(\frac{\nu+3}{2}\right)}{\sqrt{\pi}\sqrt{\nu}(x^2+\nu)\Gamma\left(\frac{\nu}{2}\right)}\left(\frac{x^2+\nu}{\nu}\right)^{-\frac{\nu+1}{2}}\\
\frac{dt}{d\nu} &= -\frac{1}{2}\frac{\Gamma\left(\frac{\nu+1}{2}\right)}{\sqrt{\pi}\sqrt{\nu}(x^2+\nu)\Gamma\left(\frac{\nu}{2}\right)}\left(\frac{x^2+\nu}{\nu}\right)^{-\frac{\nu+1}{2}} \times\\
&\left((x^2+\nu)\log\left(\frac{x^2+\nu}{\nu}\right) - (x^2+\nu)\psi\left(\frac{\nu+1}{2}\right) + (x^2+\nu)\psi\left(\frac{\nu}{2}\right) - x^2 + 1\right)
\end{aligned} \tag{9}$$

Γ being the gamma function and ψ the psi function.

References

[1] M. Guénin, S. Derelle, M. Caes, L. Rubaldo, I. Ribet-Mohamed, RTS noise detection and voltage effect on RTS in HgCdTe focal-plane arrays, J. Electron. Mater. 49 (2020) 6963–6970.

[2] C.Y.P. Chao, S.F. Yeh, M.H. Wu, K.Y. Chou, H. Tu, C.L. Lee, V. Goiffon, Random telegraph noises from the source follower, the photodiode dark current, and the gate-induced sense node leakage in CMOS image sensors, Sensors 19 (24) (2019) 5447.

[3] J. Högel, W. Schmid, W. Gaus, Robustness of the standard deviation and other measures of dispersion, Biom. J. 36 (4) (1994) 411–427.

[4] Ribet-Mohamed, I., Arounassalame, V., Nghiem, J., Caes, M., Guénin, M., Höglund, L., ... & Christol, P. (2019, May). Residual fixed pattern noise and random telegraph signal noise of a MWIR T2SL focal plane array. In *Infrared Technology and Applications XLV* (Vol. 11002, pp. 95-107). SPIE.

[5] W. Gross, T. Hierl, M.J. Schulz, Correctability and long-term stability of infrared focal plane arrays, Opt. Eng. 38 (5) (1999) 862–869.

[6] A. Kattnig, S. Thetas, J. Primot, Ensuring long-term stability of infrared camera absolute calibration, Opt. Express 23 (14) (2015) 18381–18390.

[7] T. Liu, X. Sui, Y. Wang, Y. Wang, Q. Chen, Z. Guan, X. Chen, Strong non-uniformity correction algorithm based on spectral shaping statistics and LMS, Opt. Express 31 (19) (2023) 30693–30709.

[8] C. Lu, Stripe non-uniformity correction of infrared images using parameter estimation, Infrared Phys. Technol. 107 (2020) 103313.

[9] J. Alstott, E. Bullmore, D. Plenz, powerlaw: a Python package for analysis of heavy-tailed distributions, PLoS One 9 (1) (2014) e85777.

[10] C. Zhu, R.H. Byrd, P. Lu, J. Nocedal, Algorithm 778: L-BFGS-B: Fortran subroutines for large-scale bound-constrained optimization, ACM Trans. Mathemat. Softw. (TOMS) 23 (4) (1997) 550–560.

[11] V. Arounassalame, M. Guenin, M. Caes, L. Höglund, E. Costard, P. Christol, I. Ribet-Mohamed, Robust evaluation of long-term stability of an InAs/GaSb type II superlattice midwave infrared focal plane array, IEEE Trans. Instrum. Meas. 70 (2020) 1–8.

[12] A.P. Kattnig, J. Primot, Calibration and validation by professional observers of the Mission-Quality criterion for imaging systems design, Opt. Express 16 (7) (2008) 4824–4837.

[13] Hendrickson, A. J., Haefner, D. P., Chan, S. H., Shade, N. R., & Fossum, E. R. (2024). PCH-EM: A solution to information loss in the photon transfer method. arXiv preprint arXiv:2403.04498.